Resolving the non-Arrhenius behavior of Oxygen Anion Conductivity in YSZ Using Off-Lattice and Coarse-Grained Kinetic Monte Carlo

Yi-Wen Wei[1], Shu-Hui Guan[1], Cheng Shang[1], Zhi-Pan Liu[1,2*]

[1]Collaborative Innovation Center of Chemistry for Energy Material, Shanghai Key Laboratory of Molecular Catalysis and Innovative Materials, Key Laboratory of Computational Physical Science, Department of Chemistry, Fudan University, Shanghai 200433, China

[2]State Key Laboratory of Metal Organic Chemistry, Shanghai Institute of Organic Chemistry, Chinese Academy of Sciences, Shanghai 200032, China

ABSTRACT: Solid oxide fuel cells (SOFCs) are a key clean energy technology that converts chemical energy into electricity, but the operation at low temperatures (e.g., below 1000 K) remains extremely challenging because the oxygen anion (O^{2-}) conductivity of yttria-stabilized zirconia (YSZ) electrolytes drops too rapidly with decreasing temperature. To provide deeper insights into the low-temperature transport mechanism, here we developed a combined Off-Lattice and Coarse-Grained Kinetic Monte Carlo (OC-KMC) algorithm to simulate the O^{2-} migration at 800–2000 K. Using the Y-Zr-O global neural network (G-NN) potential, we established a comprehensive reaction table from parallel Off-Lattice KMC (OL-KMC) at different temperatures, which contains 24,089 distinct minimum configurations and 621,557 elementary ion migration pathways. The OC-KMC overcomes the low-temperature conductivity prediction difficulty and predicts the ionic conductivity σ = 0.00071–0.38 S/cm at 800–1400 K, which aligns well with experimental measurements and resolves the physical origin of the abrupt drop of the low-temperature conductivity. We show that (i) the rate-determining step of O^{2-} migration corresponds to the escape event from the global minimum; (ii) the non-Arrhenius conductivity arises from the coupled, temperature-dependent decreases in the apparent activation energy and the activation entropy. This work demonstrates the power of the OC-KMC approach in resolving complex kinetics in SOFC electrolyte materials, pointing to new directions for the design of electrolyte materials.

1. INTRODUCTION

Yttria-stabilized zirconia (8YSZ)[1,2] is a key material for solid oxide fuel cells (SOFCs) because of its exceptional oxygen anion (O^{2-}) conductivity. However, 8YSZ-based SOFCs have to operate at high temperatures (~1273 K)[3] in order to achieve the best performance. This is due to the fact that the ionic conductivity of 8YSZ (0.19 S/cm at 1273 K[4]) plummets dramatically at lower temperatures (e.g., ~0.0033 S/cm at 873 K [5]), falling below the critical threshold (> 0.01 S/cm) required for practical applications. To develop intermediate-temperature SOFCs (IT-SOFCs) functioning between 873 and 1073 K[6] with reduced energy consumption, prolonged durability, and enhanced safety[7,8], great efforts have been devoted to understanding the physical origin of the sluggish O^{2-} mobility at low temperatures[9].

Figure 1 shows the hallmark non-Arrhenius behavior[4,5,10–12] of 8YSZ's ionic transport, where the conductivity drop is characterized by two distinct apparent activation energy (E_a) regimes: 0.76 eV above 1123 K and 1.09 eV below 1123 K. This reflects the fact that the oxygen transport becomes markedly slower in the low-temperature regime. Experimental studies employing direct current (DC) and alternating current (AC) impedance methods corroborate this bifurcation picture (solid squares in **Figure 1)**. For instance, Kondoh et al.[4] reported ~0.88 S/cm at 1773 K using DC measurements, and Gong et al.[12] and Vendrell et al.[5] observed conductivities as low as ~0.0022 S/cm (~848 K) and ~0.0015 S/cm (~823 K) via AC impedance, respectively.

According to classical reaction kinetics theory, the lower E_a at elevated temperatures could imply a change in the O^{2-} migration mechanism, which has been tentatively rationalized using the "Vacancy-Association Model (VAM)". The VAM model posits that O^{2-} migration is mediated by defect complexes formed between oxygen vacancies (O_v) and surrounding cations[12]. Such defect complexes might be related to specially coordinated O_v sites as both experimental and computational studies have revealed that O_v sites in 8YSZ preferentially coordinate with $+^{+}$ ions as first nearest neighbors and Y^{3+} ions as second nearest neighbors and have significant lattice distortions around the O_v [13–17]. The VAM model further hypothesizes that O_v migration at low temperatures requires overcoming both the dissociation energy of these defect complexes and the subsequent migration barrier, whereas O_v migration at high temperatures, with the defect complexes being destroyed, only needs to overcome the migration barrier[5,12,18,19]. However, the VAM model does not have a clear

atomic model for the so-called defect complex, and its underlying picture of the isolated trapping center could be invalid when applied to a concentrated solid solution such as 8YSZ[20]; importantly, it also fails to account for the lower Arrhenius pre-exponential factor (associated with apparent activation entropy) at high temperatures or explain why the transition occurs at ~1100 K (Figure 1).

It is also a formidable task for theory to examine O_v migration routes to obtain the detailed kinetic information[21] considering the extremely large number of likely O_v configurations in 8YSZ, because even the smallest 79-atom unit cell already contains C_{54}^2= 1,431 possible O_v configurations, implying many different local defect environments[22] and, therefore, a wide range of migration barriers[23]. Previous efforts have relied on computational simulation approaches to understand the mechanism, including molecular dynamics (MD)[22,24,25] and kinetic Monte Carlo (KMC)[26,27] simulations. Our previous MD simulations have provided insights into O_v migration. By using global neural network (G-NN) potentials[22] (red hollow circles in **Figure 1**), we showed that MD can accurately reproduce the experimental high-temperature conductivity (e.g., 0.51 S/cm at 1600 K vs. experimental 0.55 S/cm at 1573 K[4]), whereas the previous simulations using empirical potentials[24,25] (e.g., Born-Mayer-Huggins) underestimate these values (blue and purple hollow circles in **Figure 1**). At lower temperatures our MD predictions, however, deviate by orders of magnitude, apparently because of the insufficient sampling of rare migration events when the O_v migration is very slow. On the other hand, although the KMC method[27] could in principle circumvent this limitation of MD (orange hollow circles in **Figure 1**), the results from Lee et al. still underestimate the apparent activation energies below 1123 K significantly (~0.77 eV vs. experimental 1.09 eV). This might be caused by the approximation in the O_v diffusion pathway and the computed barrier (e.g. without considering the concerted O_v diffusion events and without calculating reaction barrier explicitly by locating the transition state).

Here we developed a combined off-lattice and coarse-grained KMC (OC-KMC) algorithm based on G-NN potential calculations to resolve O_v migration in 8YSZ. By using this KMC algorithm, we can determine the activation enthalpy ($\Delta H^{\neq}$) of key O_v diffusion reactions from tens of thousands of O_v migration pathways. The discrepancy between experimental and previous MD low-temperature kinetics is now solved, which helps clarify the physical origin of the non-Arrhenius oxygen anion conductivity behavior in 8YSZ.

2. METHODS

2.1 Bortz-Kalos-Lebowitz algorithm

In this study, we first utilized Off-Lattice KMC (OL-KMC) to sample the O_v migration events in YSZ with dynamically varying system configurations in real time. The KMC algorithm was based on the Bortz-Kalos-Lebowitz (BKL) method[28] and was modified to fit our off-lattice treatment,

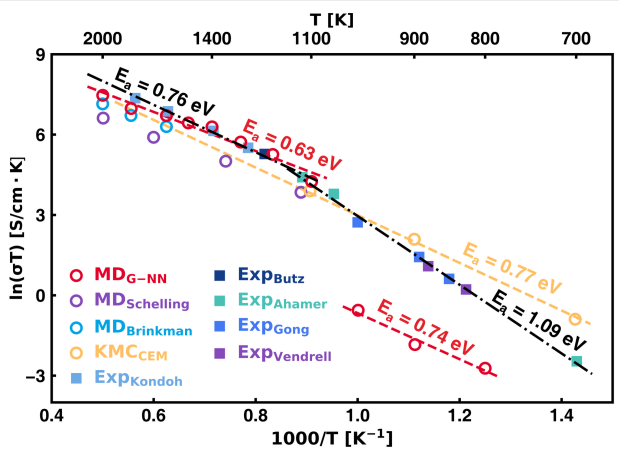

Figure 1. Arrhenius plots of the ionic conductivity of 8YSZ from literature. Hollow circles: MD results based on different potential energy surfaces (purple: BMH-Schelling[21], blue: BMH-Brinkman[22], red: G-NN potential[23]) and KMC results using the cluster-expansion approximation[25] (orange); Solid squares: Experimental results (Exp_{Kondoh}[4], Exp_{Butz}[10], Exp_{Ahamer}[11], Exp_{Gong}[12] and $Exp_{Vendrell}$[5]).

which will be detailed in Section 3.1. We now briefly introduce the BKL algorithm as follows.

Starting from a current configuration, the BKL algorithm formulates how to obtain the next system configuration and how to calculate the elapsed time interval Δt between the two configurations (X_m). According to Transition State Theory[29], for each elementary reaction **i**, an O_v migration step in this work, the rate k_i can be computed using Eq. 1,

$$k_i = \frac{k_B T}{h} \exp\left(\frac{-\Delta G^{\neq}}{RT}\right) \quad (1)$$

where k_B is the Boltzmann constant; h is Planck's constant; R is the gas constant; T is the simulation temperature; $\Delta G^{\neq}$ is the activation Gibbs free energy, which is further related to the activation enthalpy $\Delta H^{\neq}$ and the activation entropy $\Delta S^{\neq}$ as in Eq. 2:

$$\Delta G^{\neq} = \Delta H^{\neq} - T\Delta S^{\neq} \quad (2)$$

The total rate R at the current state m is the sum of all elementary reactions (n is the total number), as described in Eq. 3:

$$R_m = \sum_{i=1}^{n} k_i = \sum_{i=1}^{n} \frac{k_B T}{h} \exp\left(\frac{-(\Delta H_i^{\neq} - T\Delta S_i^{\neq})}{RT}\right) \quad (3)$$

If activation entropy is neglected as an approximation, the total rate ($\widetilde{R}_m$) simplifies to:

$$\widetilde{R}_m = \sum_{i=1}^{n} \frac{k_B T}{h} \exp\left(\frac{-\Delta H_i^{\neq}}{RT}\right) \quad (4)$$

In the BKL algorithm, the cumulative probability P_j for the elementary step j is determined by Eq. 5, where R is the total rate. The event j is selected when the condition in Eq. 6 is satisfied, where $rand_1$ is a random number within the range [0,1).

$$P_j = \frac{\sum_{i=1}^{j} k_i}{R} \quad (5)$$

$$P_{j-1} \le \text{rand}_1 \le P_j \quad (6)$$

Once the event j is selected, the KMC proceeds to the next configuration associated with the final state (FS) of the j_{th} event. The system time, t, advances by a reaction time Δt as determined by Eq. 7, where rand_2 is another random number within the range [0,1).

$$\Delta t = \frac{\ln(\text{rand}_2)}{R} \quad (7)$$

2.2 No-return acceleration to OL-KMC

In the standard BKL scheme, the event selection (Eq. 6) is weighted to favor fast, low-barrier processes. As a result, KMC sampling can become inefficient in systems with a broad distribution of barriers[30]. This can lead to rapid back-and-forth hopping between neighboring configurations with low barriers, wasting KMC steps and severely degrading the sampling efficiency in the slow, transport-relevant dynamics. To alleviate this issue without destroying the overall kinetics, we introduced a no-return modification to the OL-KMC procedure based on the characteristics of 8YSZ PES: the trajectory and the KMC clock were advanced only when a non-return transition was selected between *kinetically less important minima* (KLIM).

This approximation inevitably underestimates the residence time of these KLIM by discarding short-time recrossings. However, since KLIM intrinsically have short residence times, the no-return acceleration can be largely valid and particularly powerful for PES characterized by the following features: (i) a finite set of low-energy configurations; (ii) a vast number of high-energy configurations; and (iii) a large energetic separation between these two groups. As we show in the Results section, the global-minimum (GM) configuration in 8YSZ is separated from the non-GM configurations by a large energy gap of at least 0.6 eV. At equilibrium, this kind of PES implies a dominant equilibrium weight of the GM basin, but the Boltzmann occupation of each high energy minimum is vanishingly small. In this work, the no-return modification was applied when the system entered the non-GM network, thereby improving sampling efficiency while retaining quantitative accuracy of the kinetics. A detailed error assessment of the no-return policy is provided in Section 4.1.

2.3 Coarse-grained KMC

For low-temperature KMC, the presence of high barrier events poses substantial difficulty in obtaining converged kinetics, because the KMC clock must advance over a long time (e.g., milliseconds). To this end, given the well-separated slow and fast events in the 8YSZ PES, we further developed a Coarse-Grained KMC (CG-KMC) approach based on the OL-KMC rate data, which can efficiently propagate the slow diffusion dynamics and reproduce the OL-KMC kinetics. CG-KMC is a powerful algorithm for accelerating kinetics in systems with few well-characterized slow events but countless fast events.

The basic idea of CG-KMC is to lump all fast events along a pre-recorded trajectory into one elementary transition event. As shown in the Results section, the O^{2-} diffusion in 8YSZ frequently becomes trapped in the GM configuration, where the escape from the GM is generally the rate-determining step. Therefore, we can set the GM as the reference configuration (see Section 3.2) and lump all events from GM to GM as one excursion event, which includes a slow step (the escape reaction from GM) and many fast diffusion steps among high energy minima. The CG-KMC algorithm is described as follows.

Using OL-KMC rate data, we collected and stored all GM-to-GM excursions. For a given excursion η, the visited minima were recorded as $\{X_{\eta,m}\}_{m=0}^{L}$ with both $X_{\eta,0}$ and $X_{\eta,L}$ being GM, together with the corresponding set of total rates $\{\widetilde{R}_{\eta,m}\}_{m=0}^{L-1}$, where $\widetilde{R}_{\eta,m}$ denotes the total rate at $X_{\eta,m}$. The first step $X_{\eta,0} \rightarrow X_{\eta,1}$ (i.e., escape from the GM basin) is always the rate-limiting step of the excursion.

In CG-KMC simulations, starting from the GM, we can follow the standard KMC algorithm (Eqs. 5–6) to select an elementary event without immediately advancing time, yielding a minimum M. If M matches $X_{\eta,1}$ in an excursion η of the GM-to-GM excursion set, CG-KMC advances $\Delta t = \sum_{m=0}^{L-1} \frac{\ln(\text{rand}_m)}{\widetilde{R}_{\eta,m}}$ using Eq. 7, otherwise CG-KMC remains at the GM and re-selects an event. When multiple excursions share the same $X_{\eta,1}$, CG-KMC randomly selects one. It can be shown that, if all likely GM-to-GM excursions are used in CG-KMC to evaluate the rate, CG-KMC is equivalent to standard KMC (see SI-5).

We would like to point out that existing acceleration strategies for solving time-scale separation kinetics, such as Monte Carlo with absorbing Markov chains (MCAMC)[31] methods, have similarities with our CG-KMC. These earlier methods utilized various techniques, such as the mean-rate method (MRM)[32] and on-the-fly superbasin construction schemes (e.g. Markov-web[33,34], count-based[35], energy-based[36], and rate-threshold approaches such as bac-MRM[32,37]) to identify transient-state superbasins on the fly and estimate effective escape statistics, but their computational overhead is still high due to repeated updates and increases as the superbasin grows. In contrast, CG-KMC relies on a pre-recorded excursion library and therefore avoids on-the-fly superbasin construction and updates.

2.4 Conductivity calculation

In this work, the ionic conductivity σ was approximated from the diffusion coefficient D through the Nernst-Einstein relation in Eq. 9, where D was evaluated numerically from KMC trajectories using Eq. 10.

$$\sigma = \frac{q^2 D N}{V N_A}\left(\frac{F^2}{RT}\right) \quad (9)$$

$$D = \lim_{t\to\infty} \frac{<\Delta r(t)^2>}{6t} \quad (10)$$

In Eqs. 9–10, V is the cell volume; N_A is the Avogadro constant; q is the charge of the mobile ion (q=2 for O^{2-}); N is the number of O^{2-}; F is the Faraday constant; and $\langle \Delta r(t)^2 \rangle = \frac{1}{N}\sum_{a=1}^{N} |r_a(t) - r_a(0)|^2$ denotes the averaged mean square displacement of all individual O^{2-} ions,

where $r_a(t)$ and $r_a(0)$ are the positions of the a_{th} O^{2-} at time t and in the reference configuration, respectively.

2.5 Apparent Activation Parameters from Nernst–Einstein–Arrhenius Analysis

Combining the Nernst–Einstein relation (Eq. 9) with an Arrhenius form for the diffusivity, $D = D_0 \exp\left(-\frac{E_a^{app}}{RT}\right)$, yields

$$\sigma T = \frac{q^2 N F^2}{V N_A R} D_0 \exp\left(-\frac{E_a^{app}}{RT}\right) \quad (11)$$

Accordingly, we fit $y = \ln(\sigma T)$ as a linear function of $x = 1000/T$, $y = a + bx$, from which the apparent activation energy follows directly as

$$E_a^{app} = -b(1000R) \quad (12)$$

To extract an apparent activation entropy, we parameterize D_0 as

$$D_0 = \frac{c^2 v_0}{6} \exp\left(\frac{\Delta S_{app}}{R}\right) = \frac{\exp(a)\, V N_A R}{q^2 N F^2} \quad (13)$$

where c is the nearest-neighbor O^{2-} distance (≈2.6 Å) and v_0 is 10^{13}. This yields apparent activation entropy as

$$\Delta S_{app} = R \ln\left[\frac{6D_0}{c^2 v_0}\right] = R \ln\left[\frac{6 \exp(a)\, V N_A R}{c^2 v_0 q^2 N F^2}\right] \quad (14)$$

2.6 G-NN potential calculations

All potential energy surface (PES) calculations were performed using the LASP code—Large-scale Atomic Simulation with Neural Network Potential (www.lasphub.com)[38] with a Y-Zr-O ternary G-NN potential[21,22]. The G-NN potential was utilized in our previous MD simulations[22] to simulate the O_v migration kinetics (see Figure 1), where the high-temperature ionic conductivity agreed well with the experimental data. In this work, we used the G-NN potential to optimize the structural configurations and identify the transition states (TS). The TS was located using the double-ended surface walking (DESW) method[39], which iteratively moved two images from the initial state (IS) and FS ends towards each other until they meet and identify a TS by optimizing the highest-energy structure along the path using the Constrained Broyden Dimer (CBD) method[40]. The TS was verified by extrapolating along the reaction coordinate to ensure that the extrapolated structures correctly corresponded to the desired IS and FS.

In computing $\Delta G^{\neq}$ in Eq. 2, the activation enthalpy $\Delta H^{\neq}$ was directly obtained using the difference between the G-NN total energy of TS and that of IS, which was defined as $E_{TS} - E_{IS}$, since the zero-point-energy (ZPE) contribution and the temperature contribution to enthalpy change were small. For the activation entropy $\Delta S^{\neq}$, the activation vibrational entropy $\Delta S_{vib}^{\neq}$ was neglected in this approach.

2.7 Atomic model of 8YSZ and the algorithm to distinguish elementary events

All OL-KMC simulations used a 316-atom 8YSZ model, which is a defect-fluorite structure [41]. The structure comprises 108 cations (92 Zr^{4+} and 16 Y^{3+}) occupying face-centered cubic (fcc) sites and 208 oxygen anions (O^{2-}) distributed across 216 tetrahedral sites, resulting in 8 unoccupied sites, referred to as O_v sites.

In KMC simulations, all cations were kept fixed at the GM configuration determined in our previous work[21]. The dynamic redistribution of O_v sites during simulation served as the primary structural descriptor for differentiating system states. To quantitatively characterize these structural variations, we calculated the O_v-O_v radial distribution function (RDF) using Eq. 15:

$$g_{O_v-O_v}(r) = \frac{V}{N_{O+O_v}} \frac{\frac{1}{N_{O_v}} \sum_{a=1}^{N_{O_v}} n_{O_v}}{4\pi r^2 \Delta r} \quad (15)$$

where n_{O_v} is the number of O_v located between distances r to $r + \Delta r$ from the central O_v. g(r) is normalized by three parameters: the total number of central O_v (N_{O_v}), the number of anionic sites N_{O+O_v} in the perfect cubic lattice ($= N_O + N_{O_v}$), and V.

3. RESULTS

3.1 Elementary events from OL-KMC

As a start, we utilized the OL-KMC algorithm to model the O_v diffusion in YSZ, which is a dynamic system with very slow kinetics but complex reaction pathways. For such a system at low temperatures, MD simulations can readily be trapped in local minima due to the high barriers while traditional KMC simulations also fail because of the difficulty in capturing all reaction events that are required for constructing a reaction list.

Our OL-KMC framework circumvented these dual challenges by implementing a continuous rate list regeneration scheme, as detailed in **Figure 2(a).** The system was initiated with the GM configuration and an empty rate list, dynamically generating elementary reaction sets as the simulation progressed. At each KMC step, accessible pathways for the current IS were either retrieved from the existing rate lists or generated through the protocol outlined in **Figure 2(b).** For elementary reactions not associated with the GM, the reaction was not allowed to return to its previous configuration, implementing a no-return strategy for fast steps (see Methods 2.2 and also our reasoning in Section 3.2). The BKL algorithm selected the FS from these pathways, which then became the new IS for subsequent iterations. The collection of the events was accelerated through 9 concurrent temperature trajectories (800–2000 K), each running > 1×10^3 KMC steps per instance. Reaction information, i.e. the rate lists, across different trajectories was synchronized after every KMC step.

During KMC simulations, we recorded new configurations, i.e. new IS, and for each new IS, the subsequent O_v migration events were enumerated by analyzing atomic environments up to second-nearest neighbors (2NN). As shown in **Figure 2(b)**, the reaction generation workflow

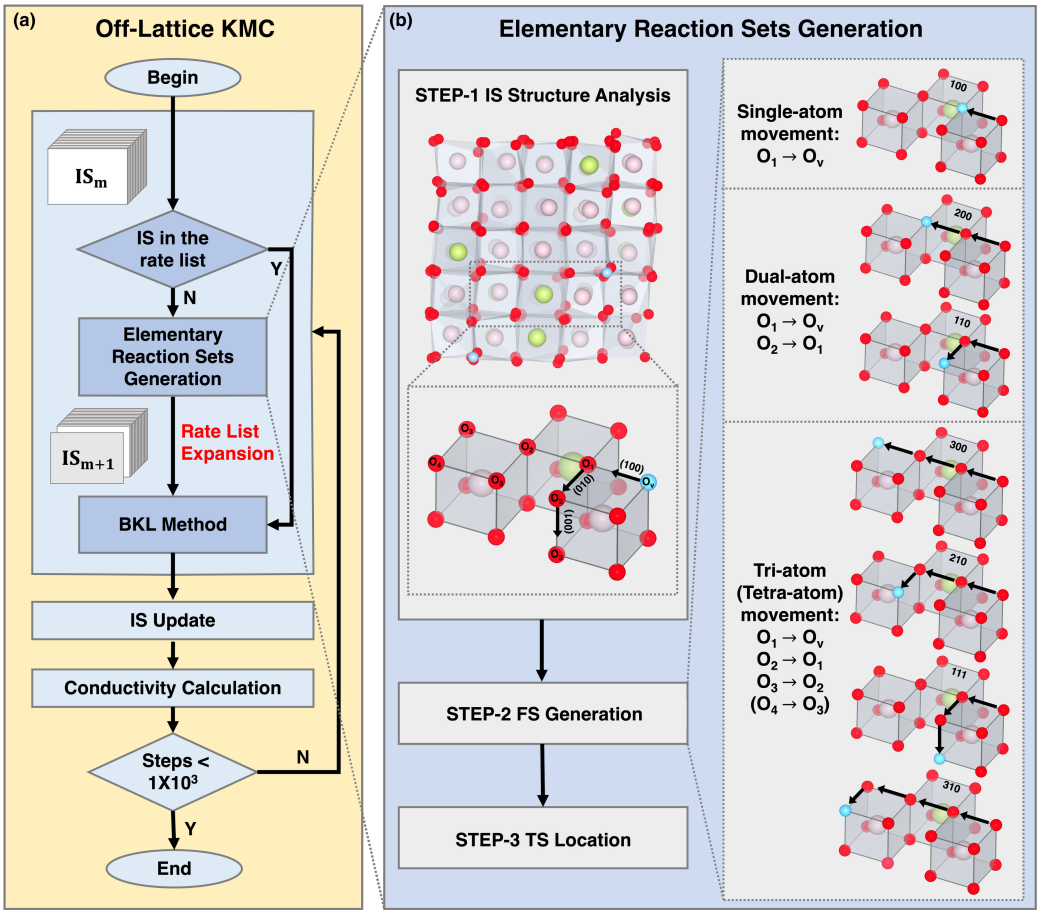

Figure 2. **OL-KMC to collect elementary events at the full-temperature range**. (a) OL-KMC algorithm flowchart (b) Elementary reaction sets generation flowchart. Red atoms: O^{2-}; Blue atoms: O_v; Pink atoms: Zr^{4+}; Green atoms: Y^{3+}; Arrows: O^{2-} movement directions.

comprises three steps. In **Step-1**, for each new IS, we identified 8 O_v, their 6 different first-neighbor (1NN) O^{2-} (O_1), and 5 additional 2NN O^{2-} sites (O_2) adjacent to each O_1. In **Step-2,** we first identified 36 likely migration ending configurations (FSs) for each O_v. Specifically, each O_v could move to one of the O_1 sites, and each O_1 site could further link to 5 possible O_2 sites, resulting in 288 possible elementary reactions (8 O_v × [6 O_1 + 6 O_1 × 5 O_2]). By considering all these FSs possibilities, the G-NN calculations were utilized to relax each FS structure to the minimum until the maximum atomic force fell below 0.05 eV/Å. In **Step-3**, distinct FSs were selected, and the TS for each IS/FS pair was located using the DESW method. Based on these new TSs, the rate $\widetilde{R}_m$ (Eq. 4) was calculated using the reaction barrier ($E_{TS} - E_{IS}$).

We may emphasize that all elementary events recorded in the OL-KMC can be categorized conceptually according to the crystallographic directions of the O_v movement. As shown in **Figure 2(b)**, the 6 1NN FSs all correspond to the O_v movement along ⟨100⟩ directions and the 30 2NN FSs correspond to either ⟨200⟩ or ⟨110⟩ directions. In addition, as our off-lattice simulation utilized the real atomic model that involved the full relaxation of FS geometry, the diffusion event could involve four types of O^{2-} collective motions, which align with ⟨111⟩, ⟨210⟩, ⟨300⟩, and ⟨310⟩ directions. For the GM structure as the IS, for instance, our pathway distribution analysis showed 20 ⟨100⟩, 28 ⟨200⟩, 72 ⟨110⟩, 8 ⟨300⟩, 52 ⟨210⟩, 12 ⟨111⟩ and 8 ⟨310⟩ directional migration events, which illustrates the complexity of O_v diffusion kinetics in YSZ.

3.2 Reaction data statistics and rate-determining transition process

From OL-KMC simulations, we identified 24,089 distinct IS configurations, along with 621,557 elementary reactions. These configurations are mapped and shown in **Figure 3(a)** using a three-dimensional visualization scheme: the x-axis quantifies the relative energy of each IS with respect to the GM configuration (E_{IS}), while the y-axis represents the minimum activation energy barrier (min-E_a) required to escape the configuration, and the color gradient encodes the temperature-dependent escape rate $\widetilde{R}$ (calculated via Eq. 4) at 800 K, ranging from slow (blue) to fast (red) transitions. Marginal density plots along the top and right edges illustrate the statistical distributions of E_{IS} and min-E_a values, respectively.

Figure 3(a) demonstrates the large energy range of O_v migration events. The IS configurations span an energy

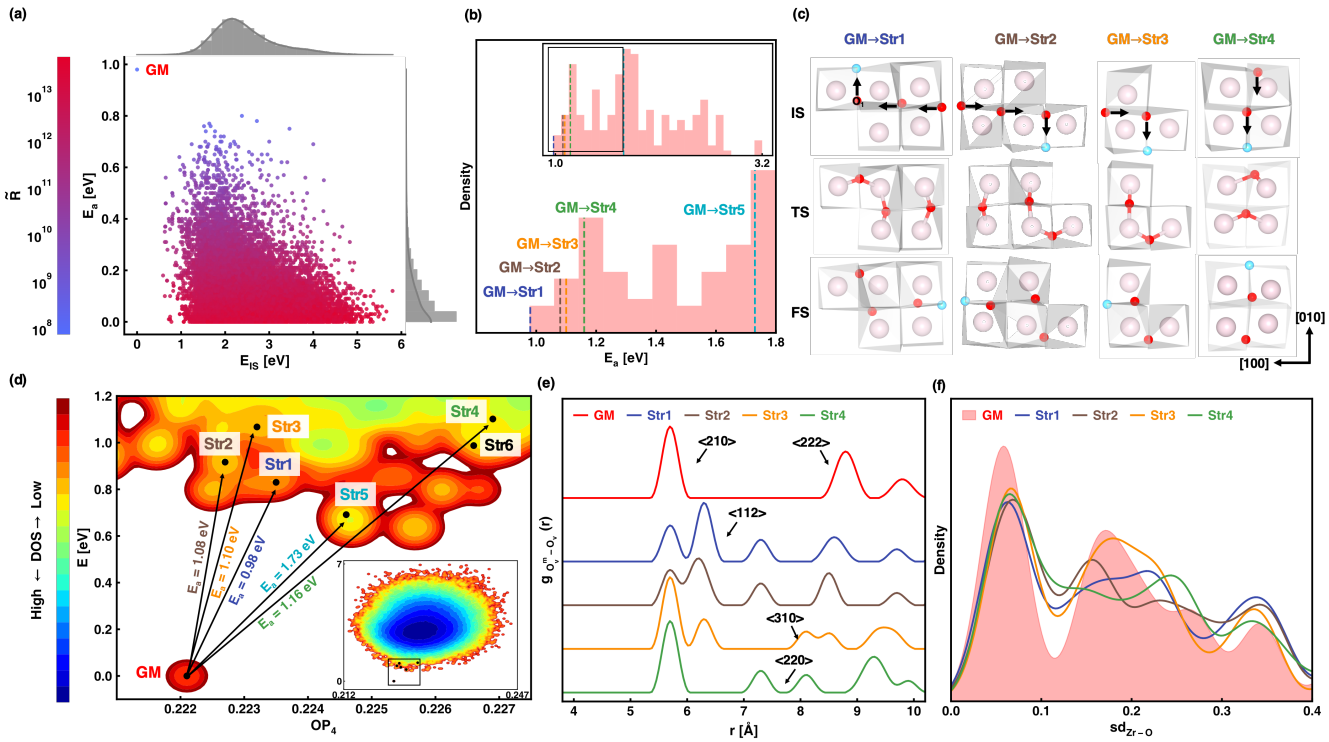

Figure 3. **Elementary events and global PES of 8YSZ from OC-KMC**. (a) 24,089 configurations in E_{IS}-E_a space with the color intensity reflecting the escape rate of the configuration calculated using at 800 K. (b) E_a distribution of GM Path with typical elementary reactions (labeled GM-Str1/2/3/4/5) highlighted in the magnified region. (c) Snapshots of the structures along the GM-Str1/2/3/4. (d) Global PES constructed using OP_4-E_{IS} descriptors, where the main panel displays low-energy configurations through contour plots, while the inset shows the complete energy range of explored PES data. Representative configurations are labeled by black dots: GM (0.2221,0.00); Str1 (0.2235,0.83); Str2 (0.2227,0.92); Str3 (0.2232,1.07); Str4: (0.2269,1.10); Str5: (0.2246,0.70); Str6: (0.2266,0.99). (e) Radial distribution function g(r) of the O_v^m-O_v pairs in GM and Str1/2/3/4, where O_v^m represents the migrating O_v during GM-based pathways GM→Str1/2/3/4. (f) KDEs of the sd_{Zr-O} for each eight-coordinate Zr^{4+} in the GM and Str1/2/3/4.

range of 0–5.8 eV, exhibiting a broad maximum around 2.0 eV, which suggests that the ISs around 2.0 eV are more often visited. By contrast, the min-E_a distribution follows an exponential decay (R^2 = 0.99 for the exponential fit; see Figure S1), with the configuration density decreasing by a factor of 646 from 0.1 eV to 0.7 eV, suggesting most elementary events have extremely low barrier, i.e. < 0.1 eV. Notably, the GM configuration requires the highest escape barrier, with min-E_a=0.98 eV, indicating that the GM is the key trapping state. Consistently, the escape rates, $\tilde{R}$, exhibit a general inverse correlation with min-E_a (Pearson's r = −0.72, Figure S2), as evidenced by the smooth color transition from red (low barrier, fast escape rate) to blue (high barrier, slow escape rate).

Among all configurations, the GM state is unique, because it is both the thermodynamic most stable minimum and the kinetically slowest minimum to escape. To gain deeper insight into the escape events from the GM basin, we analyzed all 200 elementary reactions initiated from the GM (GM Path) and summarized their E_a distribution in **Figure 3(b)**. The distribution spans 0.98–3.21 eV and peaks near 1.7 eV. Since reaction probability decreases exponentially with increasing E_a, we focused on the low-barrier (< 1.8 eV) region, which contains 106 reactions. Among them, the 16 lowest-barrier reactions (0.98–1.16 eV) account for 88% of all events in the KMC selection at 800 K. These reactions originate from four distinct reactions, GM to Str1–Str4, as illustrated in **Figure 3(b)** with E_a values indicated by the dotted color lines. They start from two chemically distinct O_v, each located at four different sites (Figure S3) and each site leading to two distinct FSs. The only difference between GM and Str1-Str4 is the position of one O_v.

These reactions are illustrated in **Figure 3(c)**, highlighting the structural evolution. In all these reactions, O^{2-} migrations avoid Zr^{4+}-Y^{3+} bonds, consistent with prior reports[24,25,42] that O^{2-} diffusion proceeds preferentially through Zr^{4+}–Zr^{4+} midpoints. In GM→Str1 and GM→Str2, three neighboring O^{2-} move cooperatively, displacing one O_v by 5.7 Å along ⟨210⟩ in total: O_1 hops along [010], whereas O_2 and O_3 pass through [100] positions (E_a = 0.98 and 1.08 eV for the two pathways, respectively). By contrast, GM→Str3 and GM→Str4 feature concerted motion of two O^{2-} with O_v migrating along ⟨110⟩ and ⟨200⟩ directions, respectively, and they have relatively higher barriers (1.10 and 1.16 eV, respectively). Additional calculations based on thermally expanded lattices show that the key barrier changes only slightly with lattice parameter,

suggesting that the rate list constructed under static-lattice conditions is a good approximation over a broad temperature range (Table S1).

To rationalize why GM Path has relatively high barriers, we plotted the PES in **Figure 3(d)** (local enlarged view) and its inset (the overall view), which was constructed by projecting all minima recorded in rate lists onto a contour map. In the map, the x-axis is a distance-weighted Steinhardt order parameter, OP_4 [43], the y-axis is the energy relative to GM, and the red-to-blue color gradient denotes the local density of states of minima (DOS). **Figure 3(d)** reveals that GM is located at the bottom of a deep, isolated energy basin with no other minimum configurations within 0–0.6 eV. Consequently, GM-initiated transitions require surmounting substantial E_a (≥0.98 eV) to reach other FSs (Str1–Str4 at > 0.8 eV), as demonstrated by the four transition pathways in **Figure 3(d)**.

The structural differences between the GM and Str1–Str4 are clarified by RDF plots constructed by taking the migrating O_v (O_v^m) as the center to identify other neighboring O_v, i.e. O_v^m-O_v, as illustrated in **Figure 3(e)**. In the GM, all 8 O_v exhibit nearly-identical O_v–O_v separation (Figure S4), suggesting a homogeneous distribution of O_v. Specifically, as illustrated in **Figure 3(e),** the GM exhibits only one sharp peak at ⟨210⟩ (5.7 Å) within an 8.5 Å radius, with each O_v having two O_v neighbors within the range, indicating that O_v are separated equally at the GM. By contrast, Str1–Str4 develop additional O_v-O_v features, including ⟨112⟩ peaks at 6.3 Å (Str1–Str3), ⟨220⟩ peaks at 7.4 Å (Str1–Str2 and Str4), and ⟨310⟩ peaks at 8.2 Å (Str3–Str4), coupled with the reduced intensity at the original 5.7 Å position.

These inhomogeneous O_v position alterations further perturb the lattice, as evidenced in **Figure 3(f).** The figure shows kernel density estimates (KDEs) for the standard deviation of the eight Zr-O bond lengths for each eight-coordinate Zr^{4+} site (sd_{Zr-O}) in GM and Str1-Str4. The GM curve exhibits a narrow and pronounced peak at low sd_{Zr-O}(< 0.1), whereas the distributions for Str1-Str4 are systematically broadened and shifted toward larger sd_{Zr-O} values, with significantly enhanced weight in the high-distortion regime (sd_{Zr-O} > 0.25). Such highly distorted coordination environments impose a large energetic penalty relative to the nearly regular coordination polyhedra in GM, thereby raising the energies of Str1-Str4 above that of GM.

3.3 Coarse-grained KMC and ionic conductivity

Analysis of the OL-KMC trajectories reveals that, over the entire temperature range considered, the system overwhelmingly resides in GM, while the sampling of high-energy configurations (non-GM configurations) decreases rapidly with decreasing temperature. As a result, below 1000 K, standard KMC simulations predominantly capture the O^{2-} hopping in the immediate vicinity of GM with rare long-distance O^{2-} diffusion.

Figure 4(a) illustrates the energy profile along a typical KMC trajectory at 1000 K, where the thick blue and red lines denote stable configurations and transition states

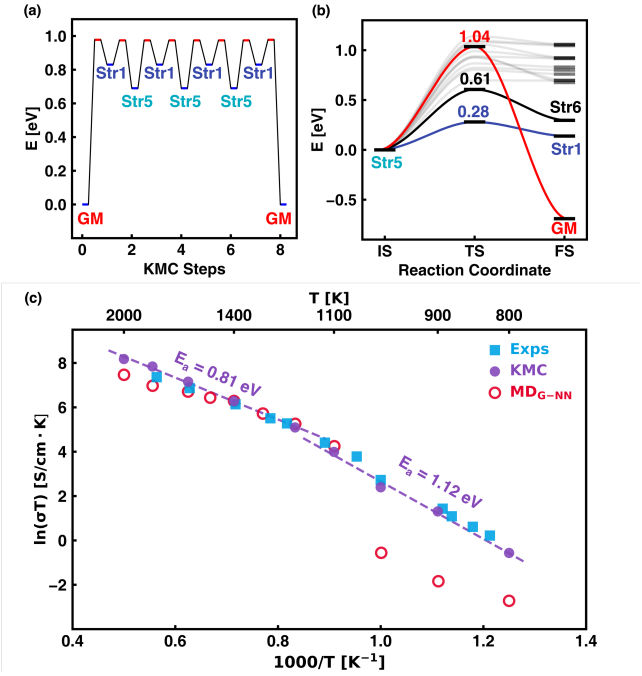

Figure 4. Energy profile and Arrhenius Plots of ionic transport in 8YSZ. (a) Energy profile along a OL-KMC trajectory at 1000 K. (b) Fifteen lowest-E_a transitions from Str5. (c) Arrhenius plots of ionic conductivity of 8YSZ based on different data. Solid purple circles: OC-KMC results; Hollow red circles: MD results based on G-NN potential; Solid blue squares: Experimental results.

(TSs), respectively. The trajectory remains strongly confined near the GM, essentially shuttling between Str1 and Str5. This pronounced localization originates from the strong kinetic bias toward returning to previously visited configurations rather than accessing new ones. Taking Str5 as an example, the fifteen lowest-E_a transition pathways are summarized in **Figure 4(b)**, among which the two lowest-barrier pathways terminate at Str1 and Str6, respectively. As shown in **Figure 3(d)**, Str1 lies in close proximity to Str5 on the global PES, whereas Str6 is separated by a higher-energy region. Consistent with this PES topology, the lower barrier for Str5→Str1 (0.28 eV), compared with Str5→Str6 (0.61 eV), leads to a transition rate ratio of approximately 42 at 1000 K, which further increases to about 110 at 800 K, rendering the escape chance from this local basin being increasingly unlikely at low temperatures. After several shuttles, Str1 eventually falls back to the GM. To overcome the severe slow kinetics in the low-temperature regime, we therefore introduced a no-return policy to the OL-KMC procedure (see Method Section 2.2). A quantitative assessment of the resulting error is provided in Section 4.1.

Using the trajectories generated by the no-return OL-KMC, we utilized the CG-KMC model, as described in Methods Section 2.3, to compute the diffusion rate of O^{2-}. CG-KMC, by coarse-graining each GM-to-GM excursion as a single event, leverages the separation of time scales in kinetics and substantially accelerates the convergence of the KMC simulations. The numbers of GM-to-GM excursions

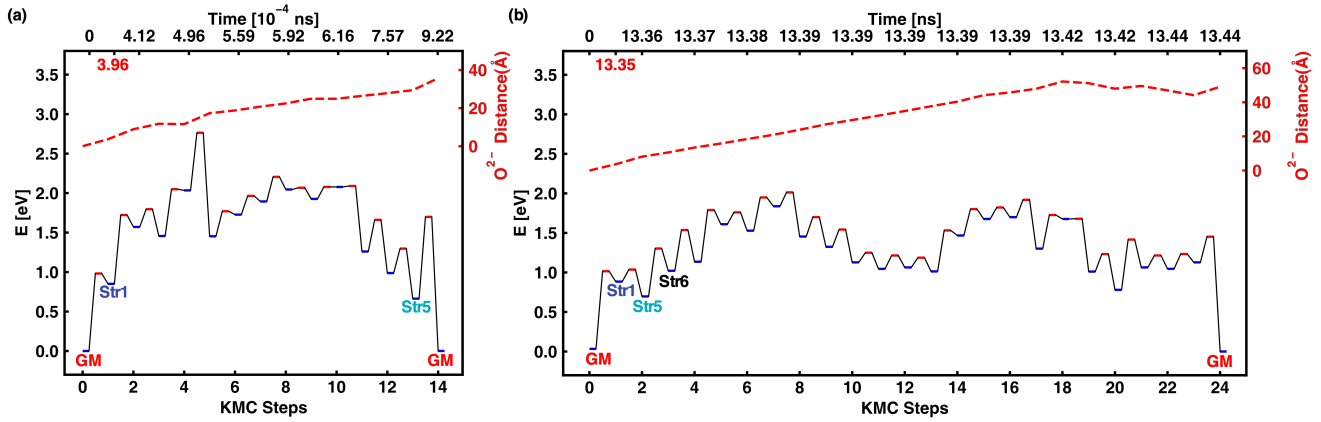

Figure 5. Energy evolution (left axis) along representative GM-to-GM excursions of the KMC trajectory at (a) 2000 K and (b) 800 K, together with the cumulative O^{2-} displacement (right axis, red dotted line)

included in the CG-KMC simulations at 2000, 1800, 1600, 1400, 1200, 1100, 1000, 900 and 800 K are 56, 42, 57, 47, 45, 57, 71, 51 and 137, respectively. The excess number at 800 K is due to the convergence check (Figure S5), which shows that the convergence of ionic conductivity is achieved above 50 GM-to-GM excursions.

Using the CG-KMC simulations, we finally obtained the O^{2-} conductivity σ at different temperatures and the KMC results (solid purple circles) are shown in **Figure 4(c)** by plotting ln(σT) vs. x = 1000/T. By comparing with experimental data (solid blue squares) and previous MD simulations (MD_{G-NN}, hollow red circles), we can summarize three key findings:

(i) KMC results accurately reproduce experimental σ in the low-temperature regime (800–1000 K), whereas MD underestimates it by ~2 orders of magnitude. This accuracy enhancement stems from KMC's capability to reach converged long-time diffusion at low temperatures: at 800 K it runs to 0.04 ms and yields a converged diffusivity (Figure S6), which is three orders of magnitude longer than the ~10 ns timescale accessible to MD.

(ii) Linear fitting of KMC data recovers dual E_a regimes observed in experiment, that is, 0.81 eV for the high-temperature regime (> 1123 K) and 1.12 eV for the low-temperature regime (< 1123 K), closely matching experimental values of 0.76 eV (> 1123 K) and 1.09 eV (< 1123 K).

(iii) Above 1600 K, the KMC simulations predict slightly higher ionic conductivity than both experiment and MD results, yielding a slightly larger apparent activation energy. This deviation originates from an underestimation of occupation probability among non-GM configurations introduced by the no-return policy, an effect that becomes increasingly significant at elevated temperatures. A detailed discussion is provided in Section 4.1.

3.4 The temperature-dependent vacancy migration pathway

We are now in a position to elucidate the temperature dependence of oxygen migration kinetics in 8YSZ. **Figures 5(a,b)** show representative GM-to-GM excursions at 2000 K and 800 K, respectively. Energy is plotted on the left y-axis, and the cumulative O^{2-} displacement (red dotted line) on the right y-axis, versus KMC steps (bottom x-axis) and the corresponding accumulated time (top x-axis). In both cases, the migration proceeds via three stages: **(i) Activation**, where the system escapes from the GM (step 0) with a sharp energy increase; this stage dominates the elapsed KMC time, accounting for 43% (3.96×10^{-4} ns) of the total excursion time at 2000 K and 99% (13.35 ns) at 800 K. **(ii) Free migration**, where O^{2-} explores a network of shallow local minima with moderate energy fluctuations; and **(iii) Recovery**, where the system returns to the GM (step 14 at 2000 K and step 24 at 800 K) accompanied by a pronounced energy drop. Notably, during stages (ii–iii) the KMC clock advances only marginally per step: the maximum single-step time contribution is ≤14% at 2000 K and ≤0.2% at 800 K.

At both temperatures, the trajectories initially follow the same escape pathway (GM→Str1) but diverge at configuration Str5. At 2000 K, the system returns directly to the GM (Str5→GM), whereas at 800 K it proceeds further to Str6. As a result, the GM-to-GM trajectory at 2000 K comprises only 14 KMC steps, significantly fewer than the 24 steps observed at 800 K, indicating a much faster recovery to the GM basin at high-temperature.

This divergence arises from the strong temperature dependence of the competition at Str5. As shown in **Figure 4(b),** the Str5→GM transition has an E_a of 1.04 eV, while the competing Str5→Str6 pathway is much lower (0.61 eV). In addition, the reverse GM→Str5 barrier is even higher (1.73 eV; Figure 3(b, d)). As a result, an immediate recovery (back to the GM) is strongly suppressed at low temperatures: the branching probability for Str5→GM is ~0.002% at 800 K but increases to ~0.89% at 2000 K where the higher-barrier return channel opens. This kinetic feature is generally true. We found that the immediate return probability from non-GM minima to the GM (Figure S6) increases from 0.7% at 800 K to 3.3% at 2000 K. Thus, once the system escapes the GM basin, it is far

more likely to continue the migration journey within the non-GM minima network at low temperatures, leading to a long GM-to-GM pathway.

4 DISCUSSION

4.1 Error analysis for the no-return policy

In the CG-KMC framework, all rates associated with GM are taken into account rigorously but the total rate of non-GM configurations is overestimated due to the no-return policy. Below we showed by derivation that the resulting overestimation of the σ is indeed negligible at low temperatures.

At equilibrium, the residence-time (occupation) probability of a configuration **m** is determined by its Boltzmann weight

$$p_m = \frac{\exp^{-\beta E_m}}{\sum_1^{all} \exp^{-\beta E_i}} \quad (16)$$

$$\beta = \frac{1}{k_B T} \quad (17)$$

The total equilibrium weight of all non-GM configurations is therefore

$$p_{non-GM} = \sum_{m \neq GM}^{all} p_m = 1 - p_{GM} \quad (18)$$

where p_{GM} denotes the equilibrium occupation probability of the GM configuration. Under the no-return algorithm, the residence time of non-GM configurations is underestimated, leading to a reduced non-GM weight $\tilde{p}_{non-GM} < p_{non-GM}$. Since σ is inversely proportional to the total time (all residence time) (Eqs. 9–10), we defined the overestimation factor Γ:

$$\Gamma = \frac{\tilde{\sigma}}{\sigma} = \frac{p_{GM} + p_{non-GM}}{p_{GM} + \tilde{p}_{non-GM}} = \frac{1}{p_{GM} + \tilde{p}_{non-GM}} \quad (19)$$

Using $\tilde{p}_{non-GM} > 0$, we obtained the upper bound

$$\Gamma \leq \Gamma_{max} = \frac{1}{p_{GM}} \quad (20)$$

Based on the occupation probabilities extracted from **Figure 3(a)**, we evaluated Γ_{max} over 800–2000 K, with the results summarized in Table S2. In the high-temperature range of 1600–2000 K, Γ_{max} lies between approximately 1.41 and 2.70, consistent with the slight overestimation of the σ by a factor of ~1.85 compared to experiment and previous MD simulations, as observed in **Figure 4(c)**. At low temperatures (≤1000 K), p_{GM} dominates the total time and Γ_{max} approaches unity. Our analysis indicates that the no-return policy error is negligible at low-temperatures, supporting the validity of the CG-KMC method.

4.2 Origin of the non-Arrhenius behavior

The O anion migration mechanism described in Sections 3.2 and 3.4 demonstrates that the anion diffusion is repeatedly restrained by an excessively deep PES valley at the GM site. This high barrier to leave GM leads to a slow activation stage and reduces the spatial extent of free-migration. These findings align with prior studies [44–46] demonstrating that PES smoothness is a critical prerequisite for achieving high ionic conductivity in materials. The poor low-temperature anion conductivity of YSZ is apparently caused by the overly stable GM configuration. This understanding offers a valuable design guideline for development of optimized solid electrolyte materials.

We can now rationalize the non-Arrhenius behavior of O^{2-} diffusion, where the barrier and entropy fitted to the low-temperature kinetic data differ from those fitted to the high-temperature data and an obvious transition appears at ~1100 K (**see Figure 1 and Figure 4(c)**). Our results show that the major difference between the O^{2-} migration at different temperatures lies in the length of GM-to-GM excursion pathway, although the rate-determining step is in fact the same. Our data do not support the conventional VAM [5,12,18,19] which proposes that lower activation barrier events are added at elevated temperatures due to the dissociation of "O_v complex". Instead, we reveal that the non-Arrhenius behavior of the ionic conductivity arises from the combined effects of both the temperature-dependent apparent activation energy, corresponding to the fitted slope of the Arrhenius plot, and the temperature-dependent apparent activation entropy, corresponding to the fitted intercept.

To identify the transition temperature, we extracted a local Arrhenius slope (effective barrier) and intercept (effective entropy) from the 800 K and 2000 K kinetic data as follows. For each temperature T_0 (800 or 2000 K) we took the corresponding KMC trajectory and re-evaluated σ(T) at $x_0 \pm \Delta x$ ($x_0 = 1000/T_0$, Δx=0.01) by recomputing KMC time increments using the total rate $\tilde{R}(T)$ defined in Eq. 4. This yielded a local linear fit of ln(σT) vs x, from which the slope and intercept at T_0 were obtained.

Interestingly, using Method 2.5, the fitted barrier (Eq. 12) and entropy (Eq. 14) at 800 K are 1.15 eV and 25.72 J mol^{-1} K^{-1}, whereas at 2000 K they decrease to 0.89 eV and 2.81 J mol^{-1} K^{-1}. By extrapolating the two lines, we obtained a transition point at 1077 K, matching well with the experimental data in Figure 1 and our simulation data in **Figure 4(c).** Compared with the high-temperature regime, the low-temperature kinetics have both higher barrier and higher entropy, which are caused by the dominance of the GM-to-Str1 step as the rate-determining step (barrier 0.98 eV) and many more structural configurations in the long GM-to-GM excursion pathway (thus higher configurational entropy).

5. CONCLUSION

In this study, we developed an OC-KMC framework to address the full-temperature-range O_v migration in 8YSZ, resolving the long-standing puzzle of temperature-dependent ionic conductivity. Rate lists of 24,089 distinct configurations and 621,557 elementary reaction pathways were generated through the simulation. This methodology shows exceptional agreement with experimental

conductivity measurements in the low-temperature regime, successfully reconciling previous discrepancies between computational models and experimental observations.

Our detailed analysis of KMC trajectories provided two key insights into O_v migration mechanisms: **(i)** The escape process from the GM constitutes the rate-determining step, which is caused by the dominant YSZ PES feature, i.e. there is a substantial energy gap (> 0.6 eV) between GM states and local minima, which creates a significant O anion migration barrier (≥ 0.98 eV); and **(ii)** the non-Arrhenius conductivity is manifested as a conductivity crossover near ~1100 K, reflecting the temperature-dependent shift in the apparent Arrhenius parameters: (E_a^{app}, ΔS_{app}) decreases from (1.15 eV, 25.72 J mol^{-1} K^{-1}) at 800 K to (0.89 eV, 2.81 J mol^{-1} K^{-1}) at 2000 K.

Given the excellent agreement between theoretical predictions and experimental results, our KMC workflow shows tremendous potential for advancing SOFC design with various material compositions over the full-temperature-range, thereby expediting the development of SOFC materials with improved ionic conductivity.

ASSOCIATED CONTENT

DATA AVAILABILITY STATEMENT

All data are available from the corresponding authors upon request.

SUPPORTING INFORMATION

This material is available free of charge via the Internet at http://pubs.acs.org, including Exponential Fit of the min-E_a Distribution**;** Inverse Correlation Between Escape Rate $\widetilde{R}$ and min-E_a**;** GM Structure and Symmetry-Equivalent O_v Sites**;** Homogeneous O_v-O_v Distance Distributions for All Eight Vacancies in the GM**;** Library-Size Convergence of CG-KMC Diffusivity**;** Time Convergence of CG-KMC Diffusivity**;** Temperature Dependence of the Immediate Return Probability to the GM Basin**;** Thermal Expansion Effect on a Key GM Escape Barrier; Upper Bound of the No-Return Overestimation Factor (Γ_{max}) Across Temperature.

ACKNOWLEDGMENT

This work was supported by the National Key Research and Development Program of China (2024YFA1509600, 2025YFA1510901), the National Science Foundation of China (12188101, U25B6005, 22033003, 92472113), the Fundamental Research Funds for the Central Universities (20720250005, 20720220011), Science & Technology Commission of Shanghai Municipality (2024ZDSYS02), the robotic AI-Scientist platform of Chinese Academy of Science, and the Tencent Foundation for XPLORER PRIZE.

REFERENCES

(1) Morimoto, T.; Nagai, M.; Minowa, Y.; Ashida, M.; Yokotani, Y.; Okuyama, Y.; Kani, Y. Microscopic Ion Migration in Solid Electrolytes Revealed by Terahertz Time-Domain Spectroscopy. *Nat. Commun.* **2019**, *10* (1), 2662. https://doi.org/10.1038/s41467-019-10501-9.

(2) Vinchhi, P. Recent Advances on Electrolyte Materials for SOFC: A Review. *Inorg. Chem. Commun.* **2023**, *152*, 110724. https://doi.org/10.1016/j.inoche.2023.110724.

(3) Huijsmans, J. P. P.; van Berkel, F. P. F.; Christie, G. M. Intermediate Temperature SOFC – a Promise for the 21st Century. *J. Power Sources* **1998**, *71* (1), 107–110. https://doi.org/10.1016/S0378-7753(97)02789-4.

(4) Kondoh, J.; Kawashima, T.; Kikuchi, S.; Tomii, Y.; Ito, Y. Effect of Aging on Yttria-Stabilized Zirconia: I. A Study of Its Electrochemical Properties. *J. Electrochem. Soc.* **1998**, *145* (5), 1527–1536. https://doi.org/10.1149/1.1838515.

(5) Vendrell, X.; West, A. R. Electrical Properties of Yttria-Stabilized Zirconia, YSZ Single Crystal: Local AC and Long Range DC Conduction. *J. Electrochem. Soc.* **2018**, *165* (11), F966. https://doi.org/10.1149/2.0881811jes.

(6) Ndubuisi, A.; Abouali, S.; Singh, K.; Thangadurai, V. Recent Advances, Practical Challenges, and Perspectives of Intermediate Temperature Solid Oxide Fuel Cell Cathodes. *J. Mater. Chem. A* **2022**, *10* (5), 2196–2227. https://doi.org/10.1039/D1TA08475E.

(7) Tarancón, A. Strategies for Lowering Solid Oxide Fuel Cells Operating Temperature. *Energies* **2009**, *2* (4), 1130–1150. https://doi.org/10.3390/en20401130.

(8) Wachsman, E. D.; Lee, K. T. Lowering the Temperature of Solid Oxide Fuel Cells. *Science* **2011**, *334* (6058), 935–939. https://doi.org/10.1126/science.1204090.

(9) Guillon, O.; Dash, A.; Lenser, C.; Uhlenbruck, S.; Mauer, G. Tuning the Microstructure and Thickness of Ceramic Layers with Advanced Coating Technologies Using Zirconia as an Example. *Adv. Eng. Mater.* **2020**, *22* (11), 2000529. https://doi.org/10.1002/adem.202000529.

(10) Butz, B.; Kruse, P.; Störmer, H.; Gerthsen, D.; Müller, A.; Weber, A.; Ivers-Tiffée, E. Correlation between Microstructure and Degradation in Conductivity for Cubic Y2O3-Doped ZrO2. *Solid State Ion.* **2006**, *177* (37), 3275–3284. https://doi.org/10.1016/j.ssi.2006.09.003.

(11) Ahamer, C.; Opitz, A. K.; Rupp, G. M.; Fleig, J. Revisiting the Temperature Dependent Ionic Conductivity of Yttria Stabilized Zirconia (YSZ). *J. Electrochem. Soc.* **2017**, *164* (7), F790. https://doi.org/10.1149/2.0641707jes.

(12) Gong, J.; Li, Y.; Tang, Z.; Xie, Y.; Zhang, Z. Temperature-Dependence of the Lattice Conductivity of Mixed Calcia/Yttria-Stabilized Zirconia. *Mater. Chem. Phys.* **2002**, *76* (2), 212–216. https://doi.org/10.1016/S0254-0584(01)00522-3.

(13) Kawata, K.; Maekawa, H.; Nemoto, T.; Yamamura, T. Local Structure Analysis of YSZ by Y-89 MAS-NMR. *Solid State Ion.* **2006**, *177* (19), 1687–1690. https://doi.org/10.1016/j.ssi.2006.02.030.

(14) Li, P.; Chen, I.-W.; Penner-Hahn, J. E. X-Ray-Absorption Studies of Zirconia Polymorphs. II. Effect of Y_2O_3 Dopant on ZrO_2 Structure. *Phys. Rev. B* **1993**, *48* (14), 10074–10081. https://doi.org/10.1103/PhysRevB.48.10074.

(15) Zacate, M. Defect Cluster Formation in M_2O_3-Doped Cubic ZrO_2. *Solid State Ion.* **2000**, *128* (1–4), 243–254. https://doi.org/10.1016/S0167-2738(99)00348-3.

(16) Fabris, S.; Paxton, A. T.; Finnis, M. W. A Stabilization Mechanism of Zirconia Based on Oxygen Vacancies Only. *Acta Mater.* **2002**, *50* (20), 5171–5178. https://doi.org/10.1016/S1359-6454(02)00385-3.

(17) Stapper, G.; Bernasconi, M.; Nicoloso, N.; Parrinello, M. ***Ab Initio*** Study of Structural and Electronic Properties of Yttria-Stabilized Cubic Zirconia. *Phys. Rev. B* **1999**, *59* (2), 797–810. https://doi.org/10.1103/PhysRevB.59.797.

(18) Li, Y.; Gong, J.; Xie, Y.; Chen, Y. Analysis of Non-Linear Arrhenius Behavior of Ionic Conduction in Cubic Zirconia Stabilized with Yttria and Calcia. *J. Mater. Sci. Lett.* **2002**, *21*, 157–159. https://doi.org/10.1023/A:1014253400747.

(19) *Diffusion in Crystalline Solids*; Murch, G. E., Nowick, A. S., Eds.; Materials science and technology series; Academic Press: Orlando, Fla, 1984.
(20) Draber, F. M.; Ader, C.; Arnold, J. P.; Eisele, S.; Grieshammer, S.; Yamaguchi, S.; Martin, M. Nanoscale Percolation in Doped BaZrO3 for High Proton Mobility. *Nat. Mater.* **2020**, *19* (3), 338–346. https://doi.org/10.1038/s41563-019-0561-7.
(21) Guan, S.-H.; Zhang, K.-X.; Shang, C.; Liu, Z.-P. Stability and Anion Diffusion Kinetics of Yttria-Stabilized Zirconia Resolved from Machine Learning Global Potential Energy Surface Exploration. *J. Chem. Phys.* **2020**, *152* (9), 094703. https://doi.org/10.1063/1.5142591.
(22) Guan, S.-H.; Shang, C.; Liu, Z.-P. Resolving the Temperature and Composition Dependence of Ion Conductivity for Yttria-Stabilized Zirconia from Machine Learning Simulation. *J. Phys. Chem. C* **2020**, *124* (28), 15085–15093. https://doi.org/10.1021/acs.jpcc.0c04331.
(23) Koettgen, J.; Grieshammer, S.; Hein, P.; Grope, B. O. H.; Nakayama, M.; Martin, M. Understanding the Ionic Conductivity Maximum in Doped Ceria: Trapping and Blocking. *Phys. Chem. Chem. Phys.* **2018**, *20* (21), 14291–14321. https://doi.org/10.1039/C7CP08535D.
(24) Devanathan, R.; Weber, W.; Singhal, S.; Gale, J. Computer Simulation of Defects and Oxygen Transport in Yttria-Stabilized Zirconia. *Solid State Ion.* **2006**, *177* (15–16), 1251–1258. https://doi.org/10.1016/j.ssi.2006.06.030.
(25) Arima, T.; Fukuyo, K.; Idemitsu, K.; Inagaki, Y. Molecular Dynamics Simulation of Yttria-Stabilized Zirconia between 300 and 2000 K. *J. Mol. Liq.* **2004**, *113* (1–3), 67–73. https://doi.org/10.1016/j.molliq.2004.02.038.
(26) Pornprasertsuk, R.; Ramanarayanan, P.; Musgrave, C. B.; Prinz, F. B. Predicting Ionic Conductivity of Solid Oxide Fuel Cell Electrolyte from First Principles. *J. Appl. Phys.* **2005**, *98* (10), 103513. https://doi.org/10.1063/1.2135889.
(27) Lee, E.; Prinz, F. B.; Cai, W. Ab Initio Kinetic Monte Carlo Model of Ionic Conduction in Bulk Yttria-Stabilized Zirconia. *Model. Simul. Mater. Sci. Eng.* **2012**, *20*, 065006. https://doi.org/10.1088/0965-0393/20/6/065006.
(28) Bortz, A. B.; Kalos, M. H.; Lebowitz, J. L. A New Algorithm for Monte Carlo Simulation of Ising Spin Systems. *J. Comput. Phys.* **1975**, *17* (1), 10–18. https://doi.org/10.1016/0021-9991(75)90060-1.
(29) Eyring, H. The Activated Complex in Chemical Reactions. *J. Chem. Phys.* **1935**, *3* (2), 107–115. https://doi.org/10.1063/1.1749604.
(30) Hein, P.; Grope, B. O. H.; Koettgen, J.; Grieshammer, S.; Martin, M. Kinetic Monte Carlo Simulations of Ionic Conductivity in Oxygen Ion Conductors. *Mater. Chem. Phys.* **2021**, *257*, 123767. https://doi.org/10.1016/j.matchemphys.2020.123767.
(31) Novotny, M. A. Monte Carlo with Absorbing Markov Chains: A Faster Monte-Carlo Algorithm for Dynamical Studies. In *Computer Simulation Studies in Condensed-Matter Physics VII*; Landau, D. P., Mon, K. K., Schüttler, H.-B., Eds.; Lotsch, H. K. V., Series Ed.; Springer Proceedings in Physics; Springer Berlin Heidelberg: Berlin, Heidelberg, 1994; Vol. 78, pp 161–165. https://doi.org/10.1007/978-3-642-79293-9_13.
(32) Puchala, B.; Falk, M. L.; Garikipati, K. An Energy Basin Finding Algorithm for Kinetic Monte Carlo Acceleration. *J. Chem. Phys.* **2010**, *132* (13), 134104. https://doi.org/10.1063/1.3369627.
(33) Boulougouris, G. C.; Frenkel, D. Monte Carlo Sampling of a Markov Web. *J. Chem. Theory Comput.* **2005**, *1* (3), 389–393. https://doi.org/10.1021/ct049900m.
(34) Boulougouris, G. C.; Theodorou, D. N. Dynamical Integration of a Markovian Web: A First Passage Time Approach. *J. Chem. Phys.* **2007**, *127* (8), 084903. https://doi.org/10.1063/1.2753153.
(35) Chill, S. T.; Welborn, M.; Terrell, R.; Zhang, L.; Berthet, J.-C.; Pedersen, A.; Jónsson, H.; Henkelman, G. EON: Software for Long Time Simulations of Atomic Scale Systems. *Model. Simul. Mater. Sci. Eng.* **2014**, *22* (5), 055002. https://doi.org/10.1088/0965-0393/22/5/055002.
(36) Pedersen, A.; Berthet, J.-C.; Jónsson, H. Simulated Annealing with Coarse Graining and Distributed Computing. In *Applied Parallel and Scientific Computing*; Jónasson, K., Ed.; Lecture Notes in Computer Science; Springer Berlin Heidelberg: Berlin, Heidelberg, 2012; Vol. 7134, pp 34–44. https://doi.org/10.1007/978-3-642-28145-7_4.
(37) Brommer, P.; Béland, L. K.; Joly, J.-F.; Mousseau, N. Understanding Long-Time Vacancy Aggregation in Iron: A Kinetic Activation-Relaxation Technique Study. *Phys. Rev. B* **2014**, *90* (13), 134109. https://doi.org/10.1103/PhysRevB.90.134109.
(38) Huang, S.-D.; Shang, C.; Kang, P.-L.; Zhang, X.-J.; Liu, Z.-P. LASP: Fast Global Potential Energy Surface Exploration. *WIREs Comput. Mol. Sci.* **2019**, *9* (6), e1415. https://doi.org/10.1002/wcms.1415.
(39) Zhang, X.-J.; Shang, C.; Liu, Z.-P. Double-Ended Surface Walking Method for Pathway Building and Transition State Location of Complex Reactions. *J. Chem. Theory Comput.* **2013**, *9* (12), 5745–5753. https://doi.org/10.1021/ct4008475.
(40) Shang, C.; Liu, Z.-P. Constrained Broyden Minimization Combined with the Dimer Method for Locating Transition State of Complex Reactions. *J. Chem. Theory Comput.* **2010**, *6* (4), 1136–1144. https://doi.org/10.1021/ct9005147.
(41) Lee, E.; Prinz, F. B.; Cai, W. Enhancing Ionic Conductivity of Bulk Single-Crystal Yttria-Stabilized Zirconia by Tailoring Dopant Distribution. *Phys. Rev. B* **2011**, *83* (5), 052301. https://doi.org/10.1103/PhysRevB.83.052301.
(42) Jaipal, M.; Chatterjee, A. Relative Occurrence of Oxygen-Vacancy Pairs in Yttrium-Containing Environments of Y2O3-Doped ZrO2 Can Be Crucial to Ionic Conductivity. *J. Phys. Chem. C* **2017**, *121* (27), 14534–14543. https://doi.org/10.1021/acs.jpcc.7b05329.
(43) Zhang, X.-J.; Shang, C.; Liu, Z.-P. Pressure-Induced Silica Quartz Amorphization Studied by Iterative Stochastic Surface Walking Reaction Sampling. *Phys. Chem. Chem. Phys.* **2017**, *19* (6), 4725–4733. https://doi.org/10.1039/C6CP06895B.
(44) Banerjee, S.; Holekevi Chandrappa, M. L.; Ong, S. P. Role of Critical Oxygen Concentration in the β-$Li_3PS_{4-x}O_x$ Solid Electrolyte. *ACS Appl. Energy Mater.* **2022**, *5* (1), 35–41. https://doi.org/10.1021/acsaem.1c03795.
(45) Mohn, C. E.; Allan, N. L.; Stølen, S. Sr and Ga Substituted Ba2In2O5: Linking Ionic Conductivity and the Potential Energy Surface. *Solid State Ion.* **2006**, *177* (3–4), 223–228. https://doi.org/10.1016/j.ssi.2005.11.006.
(46) Wang, J.; Huo, W.; Peng, Z.; Tian, Z.; Rehman, S. U.; Mei, Z.; Niu, Y.; Lv, W. Enhancement of Ionic Conductivity in NASICON-Structured $Li_3(Zr,Ti)_2(Si,Ge)_2PO_{12}$: An Ab Initio Study. *Adv. Sustain. Syst.* **2025**, *9* (4), 2401028. https://doi.org/10.1002/adsu.202401028.

TOC Graphic

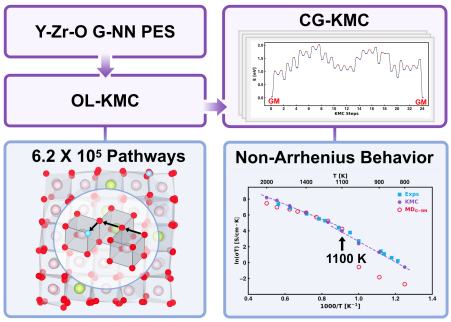
Y-Zr-O G-NN PES
OL-KMC
6.2 X 10⁵ Pathways
CG-KMC
GM
GM
Non-Arrhenius Behavior
1100 K